Limnol. Oceanogr., 50(5), 2005, 1620–1637

The degeneration of internal waves in lakes with sloping topography

L. Boegman,[1] *G. N. Ivey, and J. Imberger*
Centre for Water Research, The University of Western Australia, Crawley, Western Australia 6009, Australia

Abstract

In a laboratory study, we quantified the temporal energy flux associated with the degeneration of basin-scale internal waves in closed basins. The system is two-layer stratified and subjected to a single forcing event creating available potential energy at time zero. A downscale energy transfer was observed from the wind-forced basin-scale motions to the turbulent motions, where energy was lost due to high-frequency internal wave breaking along sloping topography. Under moderate forcing conditions, steepening of nonlinear basin-scale wave components was found to produce a high-frequency solitary wave packet that contained as much as 20% of the available potential energy introduced by the initial condition. The characteristic lengthscale of a particular solitary wave was less than the characteristic slope length, leading to wave breaking along the sloping boundary. The ratio of the steepening timescale required for the evolution of the solitary waves to the travel time until the waves shoaled controlled their development and degeneration within the domain. The energy loss along the slope, the mixing efficiency, and the breaker type were modeled using appropriate forms of an internal Iribarren number, defined as the ratio of the boundary slope to the wave slope (amplitude/wavelength). This parameter allows generalization to the oceanographic context. Analysis of field data shows the portion of the internal wave spectrum for lakes, between motions at the basin and buoyancy scales, to be composed of progressive waves: both weakly nonlinear waves (sinusoidal profile with frequencies near 10^{-4} Hz) and strongly nonlinear waves (hyperbolic–secant-squared profile with frequencies near 10^{-3} Hz). The results suggest that a periodically forced system may sustain a quasi-steady flux of 20% of the potential energy introduced by the surface wind stress to the benthic boundary layer at the depth of the pycnocline.

The turbulent benthic boundary layers located at the perimeter of stratified lakes and oceans serve as vital pathways for diapycnal mixing and transport (Ledwell and Hickey 1995; Goudsmit et al. 1997; Wüest et al. 2000). Within the littoral zone, this mixing drives enhanced local nutrient fluxes and bioproductivity (e.g., Sandstrom and Elliott 1984; Ostrovsky et al. 1996; MacIntyre et al. 1999). Indirect observations suggest that turbulent benthic boundary layers are energized by internal wave activity. In lakes, the turbulence occurs as a result of (1) bed shear induced by basin-scale currents (Fischer et al. 1979; Fricker and Nepf 2000; Gloor et al. 2000) and (2) breaking of high-frequency internal waves upon sloping topography at the depth of the metalimnion (Thorpe et al. 1972; MacIntyre et al. 1999; Michallet and Ivey 1999). While the former process is relatively well understood, the latter remains comparatively unexplored.

In lakes where the effects of the Earth's rotation can be neglected, the internal wave weather may be characterized by the relative magnitudes of the period T_i of the horizontal mode-one internal seiche and the characteristic time scale of the surface wind stress, T_w (see Stevens and Imberger 1996, their table 1 for typical values). When $T_w > T_i/4$, an approach to quasi-equilibrium is achieved, with a general thermocline tilt occurring over the length of the basin (Spigel and Imberger 1980; Stevens and Imberger 1996, and Fig. 1b, c). From this initial condition, the resulting internal wave field may be decomposed into a standing seiche, a progressive nonlinear surge, and a dispersive high-frequency internal solitary wave (ISW) packet (Boegman et al. 2005). For some lakes, $T_w \ll T_i$, and the progressive surge is believed to originate as a wind-induced wave of depression at the lee shore (see Farmer 1978, and Fig. 1d). This wave of depression will progress in the windward direction, steepening as it travels, and eventually forming a high-frequency ISW wave packet. In the absence of sloping topography, as much as 20% of the available potential energy (PE_o)—resulting from a wind forced tilt of the isopycnals at the basin scale—may be found in the ISW field (Boegman et al. 2005). This downscale energy flux has significant implications for hydrodynamic modeling. The high-frequency waves typically have wavelengths of order 100 m (Boegman et al. 2003), much smaller than the feasible grid spacing of field-scale hydrodynamic models (Hodges et al. 2000). If the high-frequency waves break upon sloping topography, between 5% and 25% (Helfrich 1992; Michallet and Ivey 1999) of the incident solitary wave energy (1% to 5% of the PE_o) may be converted by diapycnal mixing to an irreversible increase in the potential energy of the water column.

The generation and propagation of the progressive surge and ISW packet in natural systems with variable wind stress and complex topography are not clearly understood. Many long, narrow lakes and reservoirs are characterized by vertical and sloping topography at opposite ends (e.g., at dam

[1] To whom correspondence should be addressed. Present address: Coastal Engineering Laboratory, Department of Civil Engineering, Queen's University, Kingston, Ontario K7L 3N6, Canada.

Acknowledgments

The authors thank K. G. Lamb, B. R. Sutherland, E. J. Hopfinger, J. J. Riley, G. W. Wake, and two anonymous reviewers for comments and/or discussions on this work. We also thank Hervé Michallet for supplying the laboratory data shown in Fig. 10. The Lake Pusiano data were collected by the Field Operations Group at CWR and the Italian Water Research Institute—in particular we thank Diego Copetti. The wavelet software was provided by C. Torrence and G. Compo.

L.B. was supported by an International Postgraduate Research Scholarship and a University Postgraduate Award. This research was funded by the Australian Research Council and forms Centre for Water Research reference ED 1665-LB.

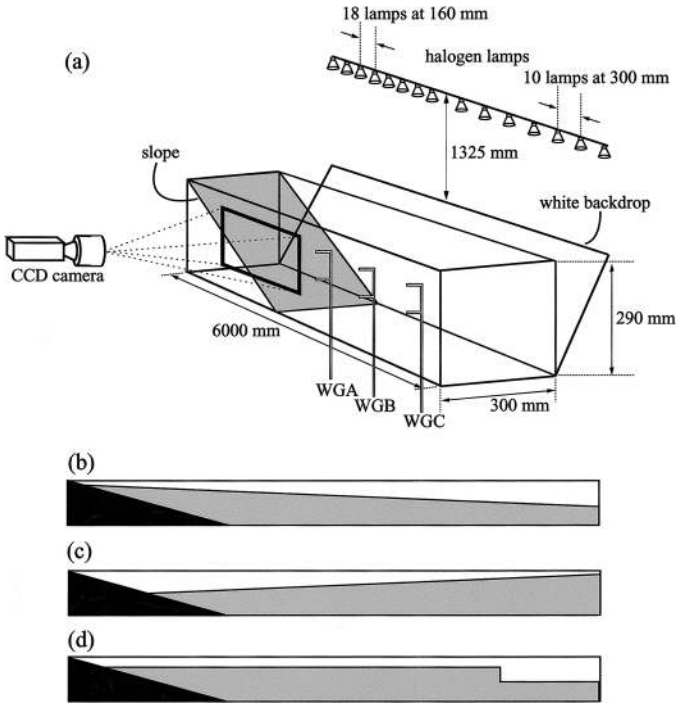

Fig. 1. (a) Schematic diagram of the experimental facility (not to scale). WG denotes ultrasonic wave gauge. See Experimental methods section for a detailed description. (b) Initial condition at $t = 0$ with upwelling at the slope. (c) Initial condition at $t = 0$ with downwelling at the slope. (d) Initial condition for the experiments by Michallet and Ivey (1999). (b–c, and d) Representative of $T_w > T_i/4$ and $T_w < T_i/4$, respectively.

walls and river mouths, respectively). The sloping bathymetry is believed to favor breaking of high-frequency waves (Thorpe et al. 1972; Hunkins and Fliegel 1973) as well as increasing the production of bed shear (Mortimer and Horn 1982), thus introducing significance to both the direction and magnitude of wind-stress, which sets up the initial thermocline displacement. For a complete understanding of the system, this directionality must be coupled with the T_w, T_i, and the steepening timescale, T_s (defined following).

In this study, laboratory experiments and field observations are used to examine the dynamics of the large-scale wave-degeneration process in a rectangular, stratified basin with sloping topography. Our objectives are to quantify the energy loss from the breaking of the ISW packets as they shoal and to cast the results in terms of parameters that are external to the evolving sub–basin-scale flow (e.g., wind speed and direction, boundary slope, quiescent stratification, etc.). This will facilitate engineering application and parameterization into field-scale hydrodynamic models. We first present the relevant theoretical background. The laboratory experiments are then described, followed by a presentation of results. Finally, the results are summarized and placed within the context of what is presently known about the energetics of stratified lakes.

Theoretical background

During the summer months, a stratified lake will typically possess a layered structure consisting of an epilimnion, metalimnion, and hypolimnion. If the vertical density gradient is abrupt through the metalimnion, the lake may be approximated as a simple two-layer system of depth h_1 and density ρ_1 over depth h_2 and density ρ_2, where $H = h_1 + h_2$ is the total depth and L denotes the basin length (e.g., Heaps and Ramsbottom 1966; Thorpe 1971; Farmer 1978). Internal waves may be initiated within a stratified lake by an external disturbance, such as a surface wind stress, τ (e.g., Fischer et al. 1979, p. 161). This stress advects surface water toward the lee shore, thus displacing the internal layer interface through a maximum excursion η_o as measured at the ends of the basin. The excursion is dependent on the strength and duration of the wind event. A steady-state tilt of the interface is achieved for $T_w > T_i/4$, allowing η_o to be expressed in terms of the shear velocity $u_* = \sqrt{\tau/\rho_o}$ as

$$\eta_o \approx \frac{Lu_*^2}{g'h_1} \tag{1}$$

where ρ_o is a reference density and $g' = g(\rho_2 - \rho_1)/\rho_2$ is the reduced gravity at the interface (see Spigel and Imberger 1980; Monismith 1987).

The internal response of the waterbody to a forcing event can be gauged by the ratio of the wind-disturbance force to the baroclinic restoring force (Spigel and Imberger 1980). Thompson and Imberger (1980) quantified this force with the Wedderburn number, which is given for our two-layer system in terms of Eq. (1) as

$$W^{-1} = \frac{\eta_o}{h_1} \tag{2}$$

Weak initial disturbances ($W^{-1} < 0.3$) will excite a standing seiche that is well described by the linear wave equation (Mortimer 1974; Fischer et al. 1979; Boegman et al. 2005). The periods of this seiche for a two-layer system are

$$T_i^{(n)} = \frac{2L}{nc_o} \tag{3}$$

where $n = 1,2,3$, etc., denotes the horizontal mode (herein the fundamental timescale; T_i, without superscript, is used to represent the gravest mode, where $n = 1$) and $c_o = \sqrt{(g'h_1h_2)/(h_1 + h_2)}$ is the linear long-wave speed.

Moderate forcing ($0.3 < W^{-1} < 1.0$) results in the development of a nonlinear surge and dispersive solitary wave packet (Thorpe 1971; Horn et al. 2001). The temporal development of the surge may be quantified by the nonlinearity parameter defined by Boegman et al. (2005) as

$$\frac{a\alpha}{c_o} \sim \frac{3\eta_o}{2}\frac{|h_1 - h_2|}{h_1h_2} \tag{4}$$

where we have used the wave amplitude scaling $a \sim \eta_o$ (e.g., Horn et al. 1999) and the nonlinear coefficient $\alpha = (3/2)c_o(h_1 - h_2)/(h_1h_2)$ (Djordjevic and Redekopp 1978; Kakutani and Yamasaki 1978). If the interface is at middepth, α vanishes, steepening cannot occur, and there is no production of solitary waves. As the progressive nonlinear surge steepens, its length scale decreases until nonhydrostatic effects become significant and the wave is subject to dispersion (see Ham-

mack and Segur 1978). This occurs as $t \rightarrow T_s$, the steepening timescale (Horn et al. 2001)

$$T_s = \frac{L}{\alpha \eta_o} \tag{5}$$

Steepening is eventually balanced by dispersion and the surge degenerates into a high-frequency ISW packet. Internal solitary waves may be modeled to first order by the weakly nonlinear Korteweg–de Vries (KdV) equation

$$\frac{\partial \eta}{\partial t} = c_o \frac{\partial \eta}{\partial x} + \alpha \eta \frac{\partial \eta}{\partial x} + \beta \frac{\partial^3 \eta}{\partial x^3} = 0 \tag{6}$$

where $\eta(x,t)$ (positive upward) is the interfacial displacement and the dispersive coefficient $\beta = (1/6)c_o h_1 h_2$. A particular solution to Eq. (6) is the solitary wave equation (Benney 1966),

$$\eta(x - ct) = a \operatorname{sech}^2\left(\frac{x - ct}{\lambda}\right) \tag{7}$$

where the phase velocity, c, and horizontal length scale are given by

$$c = c_o + \frac{1}{3}\alpha a \tag{8a}$$

$$\lambda^2 = \frac{12\beta}{a\alpha} \tag{8b}$$

Note the functional dependence between λ and a for the nonlinear waves.

Breaking of high-frequency ISWs may occur if the waves propagate along the density interface into coastal regions with sloping topography. Off-shore, the interface is typically positioned such that $h_1 < h_2$ and $\alpha < 0$, resulting in ISWs of depression. As a bounded slope is approached, the shoaling waves will encounter a turning point, where $h_2 = h_1$ and $\alpha = 0$. Beyond the turning point, $h_1 > h_2$ and $\alpha > 0$, causing the ISW to change polarity and become waves of elevation. Analytical KdV theories (see Miles 1981 for a review) have been extended to model the evolution and propagation of solitary waves when the topography and background flow are slowly varying (e.g., Lee and Beardsley 1974; Djordjevic and Redekopp 1978; Zhou and Grimshaw 1989). Horn et al. (2000) further extended these theories to a strong space–time varying background, but propagation through the turning point and wave breaking were necessarily avoided. First-order analytical models do not allow transmission of the ISWs through the singular point at $\alpha = 0$.

The location of the turning point may be easily obtained for a quiescent two-layer flow with sloping topography in the lower layer. Define the thickness of the lower layer along the slope in x as

$$h_2(x) = H - h_1 - \left(\frac{H}{L_s}\right)x \tag{9}$$

where L_s denotes the slope length and $x = 0$ at the toe of the slope. The location of the turning point on the slope is given in nondimensional form by letting $h_2(x) = h_1$

$$\frac{x}{L_s} = \frac{h_2 - h_1}{H} \tag{10}$$

As a wave travels along the slope, it steepens, a increases, and the streamlines approach vertical. During steepening, the maximum horizontal fluid velocity in the direction of wave propagation u_{max} will increase more rapidly than c and a limiting amplitude may be achieved where the velocities in the wave crest become equal to the phase velocity. Here, this limit is defined as the breaking limit and the location on the slope where this limit is observed is the breaking point.

The type of internal wave breaking that occurs at the breaking point may be inferred by analogy to surface breakers. Of the continuum of surface breaker types that exists, four common classifications are used (see Komar 1976). Spilling breakers occur on mildly sloping beaches where steep waves gradually peak and cascade down as white water. Plunging breakers are associated with steeper beaches and waves of intermediate steepness, the shoreward face of the wave becomes vertical, curling over and plunging forward as an intact mass of water. Surging breakers occur on steep beaches where mildly sloping waves peak up as if to plunge, but the base of the wave surges up the beach face. Collapsing breakers, which mark the transition from plunging to surging, begin to curl over and then collapse upon themselves with some of the water mass surging forward up the slope.

For surface waves, Galvin (1968) and Battjes (1974) found that the ratio of the beach slope S to the wave slope (a/λ) was suitable for classifying the breaker type. This ratio is expressed as either off-shore or near-shore forms of the Iribarren number ξ,

$$\xi_b = \frac{S}{(a_b/\lambda_\infty)^{1/2}} \tag{11a}$$

$$\xi_\infty = \frac{S}{(a_\infty/\lambda_\infty)^{1/2}} \tag{11b}$$

where the subscripts ∞ and b refer to off-shore and near-shore wave properties, respectively (Fig. 2a,b). The breaker height a_b is measured when the wave face first becomes vertical in the surf zone.

The dynamics of internal wave breaking on sloping topography have been classified according to the ratio of λ_∞ to the slope length, L_s (e.g., Michallet and Ivey 1999; Bourgault and Kelley 2003). This parameter retains no knowledge of the actual boundary slope and consequently may not be used to generalize results. This is shown in Fig. 2c,d, where, in both diagrams, λ_∞/L_s is equivalent, yet $H_1/L_s \neq H_2/L_s$ and different breaking dynamics are expected as the internal waves shoal. The utility of the ratio of the beach slope to the internal wave slope has been suggested (e.g., Legg and Adcroft 2003), but a formal classification based on internal wave data has yet to be performed. Perhaps this stems from the difficulty in measuring the parameters a_b, λ_∞, and a_∞ for internal waves. It is preferable to recast ξ in terms of readily

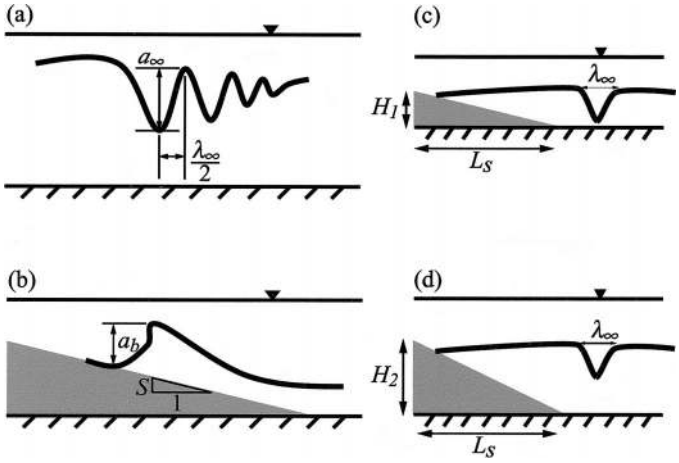

Fig. 2. Schematic diagram of wave and slope properties: Off-shore wave amplitude, a_∞, off-shore wavelength, λ_∞, near-shore breaker height, a_b, boundary slope, S, slope-length, L_s, and slope-height, H_1 and H_2.

measured variables (e.g., wind speed, quiescent fluid properties). This is accomplished for ISWs with a sech^2 profile by noting that the wave slope $a_\infty/\lambda_\infty \sim \alpha\eta_o/c_o$, resulting in

$$\xi_{\text{sech}} = \frac{S}{(\alpha\eta_o/c_o)^{1/2}} \tag{12}$$

where η_o is easily estimated using (1). Similarly, for sinusoidal waves $a_\infty/\lambda_\infty \sim f\eta_o/c_o$ giving

$$\xi_{\text{sin}} = \frac{S}{(f\eta_o/c_o)^{1/2}} \tag{13}$$

In the following sections, progressive sinusoidal waves are addressed and the wave frequency, f, is discussed.

Experimental methods

The experiments were conducted in a sealed rectangular acrylic tank (600 cm long, 29 cm deep, and 30 cm wide) into which a uniform slope of either 1/10 or 3/20 was inserted, extending the entire height of the tank and positioned at one end (Fig. 1). The tank was filled with a two-layer stratification from reservoirs of fresh and saline filtered water (0.45-μm ceramic filter). For visualization purposes, the lower layer was seeded with dye (Aeroplane Blue Colour 133, 123). Prior to commencing an experiment, the tank was rotated to the required interfacial displacement angle. From this condition, the setup and subsequent relaxation from a wind-stress event was simulated through a rapid rotation of the tank to the horizontal position, leaving the interface inclined at the original angle of tilt of the tank. Depending on the initial direction of rotation prior to commencing an experiment, the resulting inclined interface at $t = 0$ could be characterized as either upwelling on the slope (Fig. 1b) or downwelling on the slope (Fig. 1c). The ensuing vertical displacements of the density interface $\eta(x,t)$ were measured using three ultrasonic wave gauges (Michallet and Barthélemy 1997) distributed longitudinally along the tank at locations A, B, and C (Fig. 1). The wave gauges logged data to a personal computer at 10 Hz via a 16-bit analog-to-digital converter (National Instruments PCI-MIO-16XE-50). The experimental variables considered in this study, together with the resolution with which they were determined, are given in Table 1.

To visualize the interaction of the internal wave field with the sloping topography, digital images with a resolution of 1 pixel per mm were acquired at a rate of 5 Hz from a progressive scan CCD camera (PULNiX TM-1040) equipped with a manual zoom lens (Navitar ST16160). In-

Table 1. Summary of experimental runs. The experimental variables together with the resolution with which they were determined: the slope, S, the interface depth, h_1 ($\pm$0.2 cm), the maximum interface displacement, η_0 ($\pm$0.2 cm), the horizontal mode one basin-scale internal wave period (T_i), the steepening time scale (T_s), and the density difference between the upper and lower layers, $\Delta\rho \approx 20$ kg m^{-3} ($\pm$2 kg m^{-3}). The η_0 values were measured along the vertical end wall, where the + and − symbols denote an initial displacement as measured above and below the quiescent interface depth, respectively (i.e., + as in Fig. 1c and − as in Fig. 1b).

Run	S	h_1/H	W^{-1}	T_i (s)	T_s (s)	Run	S	h_1/H	W^{-1}	T_i (s)	T_s (s)
1	3/20	0.19	−0.39	130	146	19	1/10	0.19	−0.26	130	218
2	3/20	0.18	−0.86	133	66	20	1/10	0.20	−0.81	128	70
3	3/20	0.21	−0.93	126	61	21	1/10	0.19	−0.85	130	67
4	3/20	0.29	−0.38	113	167	22	1/10	0.30	−0.23	112	283
5	3/20	0.29	−0.58	113	109	23	1/10	0.30	−0.50	112	130
6	3/20	0.29	−0.90	113	71	24	1/10	0.27	−0.92	115	66
7	3/20	0.47	−0.35	102	862	25	1/10	0.51	−0.29	102	2,880
8	3/20	0.47	−0.73	102	413	26	1/10	0.51	−0.59	102	1,416
9	3/20	0.48	−0.90	102	493	—	—	—	—	—	—
10	3/20	0.20	+0.43	128	132	27	1/10	0.20	+0.15	128	379
11	3/20	0.19	+0.62	130	92	28	1/10	0.20	+0.85	128	67
12	3/20	0.20	+0.86	128	66	29	1/10	0.20	+1.0	128	57
13	3/20	0.30	+0.34	112	191	30	1/10	0.27	+0.25	115	244
14	3/20	0.30	+0.60	112	108	31	1/10	0.30	+0.50	112	130
15	3/20	0.30	+0.86	112	76	32	1/10	0.30	+0.91	112	72
16	3/20	0.49	+0.29	102	2,997	33	1/10	0.51	+0.29	102	2,880
17	3/20	0.50	+0.41	102	—	34	1/10	0.51	+0.66	102	1,265
18	3/20	0.50	+0.82	102	—	—	—	—	—	—	—

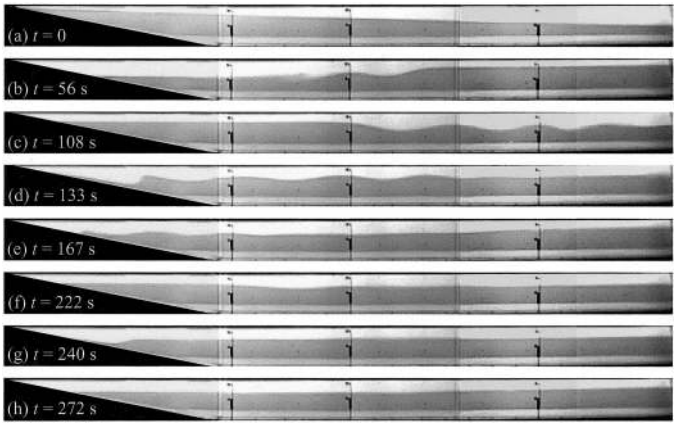

Fig. 3. Video frames showing the wave field evolving from the initial condition in (a). The surge and ISW packet are propagating to the right in (b) and to the left in (c), (d), (f), and (g). Wave breaking is shown to occur upon the slope. For this experiment, $h_1/H = 0.29$ and $\eta_o/h_1 = 0.90$. The apparent dye-free layer near the tank bottom is a spurious artifact of light reflection.

dividual frames were captured in a LabVIEW environment from a digital frame grabber (National Instruments PCI-1422) and written in real-time to disk. The tank was illuminated with backlight from twenty-eight 12-V, 50-W halogen lamps (General Electric Precise MR16; Fig. 1). To remove flicker associated with the AC cycle, a constant DC supply was maintained to the lamps via four 12-V car batteries. The images were corrected for vignetting, variations in illumination intensity, dust, and aberrations within the optical system and pixel gain and offset following the methods of Ferrier et al. (1993). This procedure required flat-field composite images of (1) the room darkened and the lens cap on the camera (dark image), as well as (2) the tank filled with dyed saline water from the reservoir (blue image), and (3) filtered tap water (white image). From the three flat-field image composites, a linear regression was performed on the gray scale response at each pixel location versus the mean pixel response across the CCD array to yield slope and intercept arrays. The experimental images were subsequently corrected at each pixel by subtracting the dark image, subtracting the intercept array, and dividing by the slope array (e.g., Cowen et al. 2001). Note that a correction for light attenuation was not required as a result of the backlight geometry. The gray scale pixel response within each image was then calibrated to the fluid density by associating measured densities in the fluid layers with the mean corrected pixel response of the blue and white images and mapping the intermediate values according to the log-linear dye versus concentration relationship, as determined from an incremental calibration procedure in a test cell.

Results

Flow field—To illustrate the qualitative features of the flow, let us concentrate on the behavior of a particular experiment (run 6, Table 1). From the initial condition, as shown in Fig. 3a, the flow was accelerated from rest by the baroclinic pressure gradient generated by the initial tilted

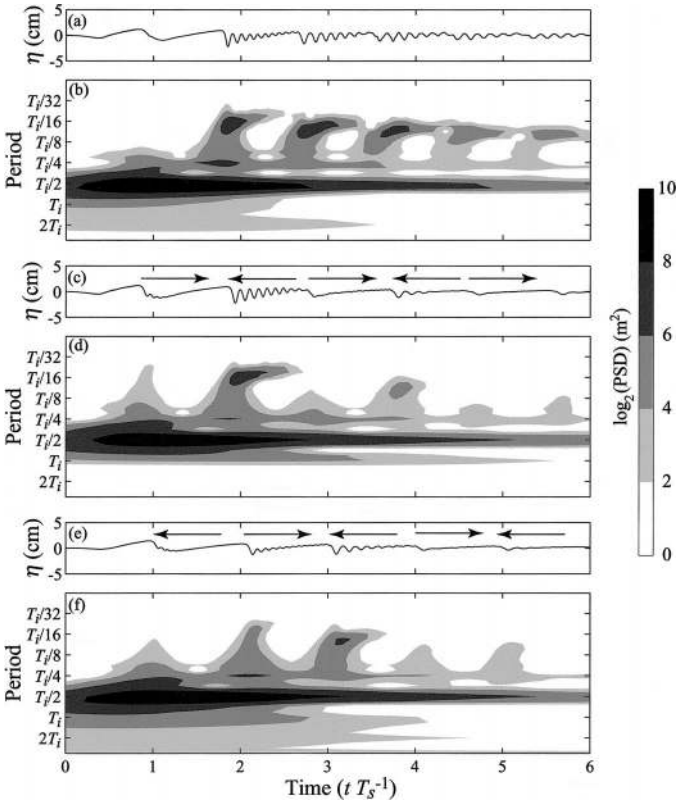

Fig. 4. (a) Time series and (b) continuous wavelet transforms showing the temporal evolution of the internal surge and solitary wave packet for the case of no slope (case 1). (c,d) Same as (a) and (b) except for the initial condition of upwelling on the 3/20 slope (case 2). (e,f) Same as (a) and (b) except for the initial condition of downwelling on the 3/20 slope (case 3). For all experiments, $\eta_o/h_1 \approx 0.7$, $h_1/H \approx 0.2$, and $T_s \approx 70$ s. The arrows in (c) and (e) denote the direction of wave propagation relative to the tank schematics shown in Fig. 1c,d, respectively.

density interface. Characteristic of a standing horizontal mode-one (H1) seiche, the lower layer moved toward the downwelled end of the tank with a corresponding return flow in the upper layer. Progressing initially from left to right, an internal surge and ISW packet were also evident (Fig. 3b). These reflected from the vertical end wall and progressed left toward the slope (Fig. 3c). The ISWs subsequently shoaled upon the topographic slope and wave breaking was observed (Fig. 3d,e). Not all wave energy was dissipated at the slope, as a longwave was reflected (Fig. 3e, right side of tank). This was reflected once again from the vertical wall and a secondary breaking event was observed (Fig. 3g). After the secondary breaking event, the internal wave field was relatively quiescent (Fig. 3h).

The frequency content of the internal surge and ISW packet, as well as the effects of the directionality associated with the initial forcing condition (i.e., upwelling or downwelling on the slope), were examined through a time–frequency analysis carried out using continuous wavelet transforms (Torrence and Compo 1998). Results from wavegauge B, a nodal location for the H1 seiche, are shown for three representative experiments (Fig. 4), where the forcing ampli-

tude, $\eta_o/h_1 \approx 0.7$, and layer thickness, $h_1/H \approx 0.2$, were similar. Case 1 is a reference case with no slope (Fig. 4a,b). The majority of the energy was initially found in the progressive surge with a period of $T_i/2$. For $t/T_s \geq 1$, the energy appeared to be transferred directly from the surge to solitary waves with a period near $T_i/16$; there was no evidence of energy cascading through intermediate scales (cf. Horn et al. 2001; Boegman et al. 2005). The ISW packet persisted until $t/T_s > 6$, the wave period gradually increasing from $T_i/16$ to $T_i/8$ as the rank-ordered waves in the packet separate according to Eq. (8a). The waves were eventually dissipated by viscosity. In case 2, the initial condition of upwelling on the slope (Fig. 4c,d) is as shown in Fig. 1b. The ISW packet initially evolved in the same manner as case 1, for a small time. However, over $2 < t/T_s < 3$, the fully developed ISW packet interacted with the sloping topography and rapidly lost its high-frequency energy to wave breaking (see Fig. 3). The reflected long wave, shown progressing to the right at $t/T_s \approx 3$, traveled the tank length and continued steepening. A second ISW packet was observed to develop and was observed to break over $4 < t/T_s < 5$. Case 3 is the initial condition of downwelling on the slope (Fig. 4e,f), as shown in Fig. 1c. In this experiment, the ISW packet initially interacted with the slope at $t/T_s \approx 1$. At this time, the wave packet was in the early stages of formation and only a weak breaking event, with little apparent energy loss from the wave, was observed. The reflected wave packet then continued to steepen as it propagated to the right and reflected off the end wall. Again, a second breaking event was observed over $3 < t/T_s < 4$, with more significant energy loss from the wave. From these results in closed systems, it is clear that the nature of the surge and ISW packet life history is dependent not only on the bathymetric slope but also on the direction of the forcing relative to the position of the topographic feature.

This concept is illustrated in Fig. 5, where visualization of the laboratory experiments (e.g., Fig. 3) has allowed the wave degeneration process, from the initial conditions shown in Fig. 1b,c, to be conceptually depicted. A longwave initially propagates from the upwelled fluid volume (Fig. 5b and h). This wave steepens as it travels, thus producing high-frequency ISWs. The wave groups reflect from the vertical wall with minimal loss and break as they shoal along the bathymetric slope. The breaking process is expected to be governed by ξ.

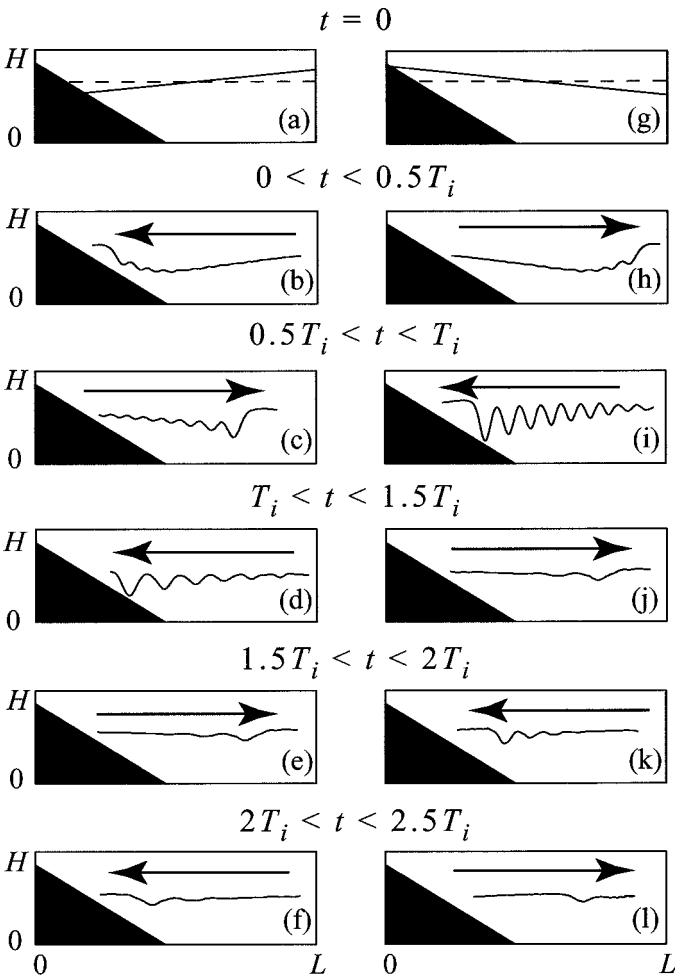

Fig. 5. Schematic illustration showing the evolution of the spatial wave profile as observed in the laboratory. (a–f) Evolution from the initial condition in Fig. 1c, g–l. Evolution from the initial condition in Fig. 1b. Illustrations are representative of $T_i/2$ time intervals. Arrows denote wave-propagation direction.

Internal solitary wave energetics—In the preceding section, a qualitative description of the wave–slope dynamics in a closed basin was presented. To quantify the temporal evolution of the ISW energy and the energy loss from these waves as they interact with the topographic boundary slope, we applied the signal processing methods of Boegman et al. (2005). This technique requires the energy in the various internal modes to be discrete in frequency space (as demonstrated in Fig. 4), thus allowing the individual signals to be isolated through selective filtering of the interface displacement time series. By assuming an equipartition between kinetic and potential forms of wave energy, the energy in the surge (E_{NS}) and ISW wave packets (E_{ISW}) was determined from the filtered time series as the integral of the signal over the wave/packet period. Note that net downscale energy flux through wave breaking at the boundary may not be quantified by this method because we cannot account for the observed upscale energy flux to reflected longwaves. Results are presented in Fig. 6, showing contours of E_{NS}/PE_o (Fig. 6a) and E_{ISW}/PE_o (Fig. 6b–f). In each panel, the vertical axis ($\alpha\eta_o/c_o$) indicates the relative magnitudes of the linear and nonlinear components of the internal wave field (from Eq. (4)), while the horizontal axis (T_i) reveals how the system evolves in time. The times at which the solitary wave packet shoals upon the sloping beach and T_s are also indicated (see caption).

For case 1, where there is no slope, the surge energy (E_{NS}/PE_o) is shown to increase during an initial nonlinear steepening phase ($0 < t \leq T_s$) and retain up to 20% of the PE_o at $t \approx T_s$ (Fig. 6a). When $t > T_s$, the E_{NS}/PE_o decreased from this maximum, with a corresponding increase in ISW energy, until eventually all of the surge energy was transferred to the solitary waves with little loss (Fig. 6b). In the absence

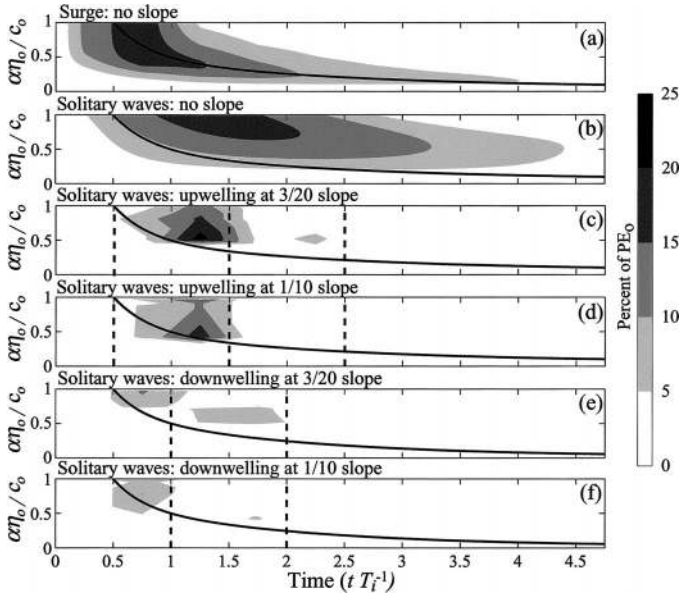

Fig. 6. General evolution of internal wave energy normalized by the PE_o introduced at the initial condition: (a) Surge energy (i.e., E_{NS}/PE_o) and (b) ISW energy (i.e., E_{ISW}/PE_o) for the case of no slope. The contours in (a) and (b) are least squares fit to the data (see Boegman et al. 2004, 2005). ISW energy for the case of (c) upwelling along the 3/20 slope and (d) upwelling along the 1/10 slope. ISW energy for the initial condition of (e) downwelling along the 3/20 and (f) downwelling along the 1/10 slope. Contours are presented as a percentage of the PE_o introduced at $t = 0$ and are compiled using the data in Table 1 and Boegman et al. (2005). The contour interval is 5%. The ratio T_s/T_i is indicated (solid line) for a particular $\alpha\eta_o/c_o$. The times at which the solitary wave packet shoals upon the sloping beach are also shown (dashed line).

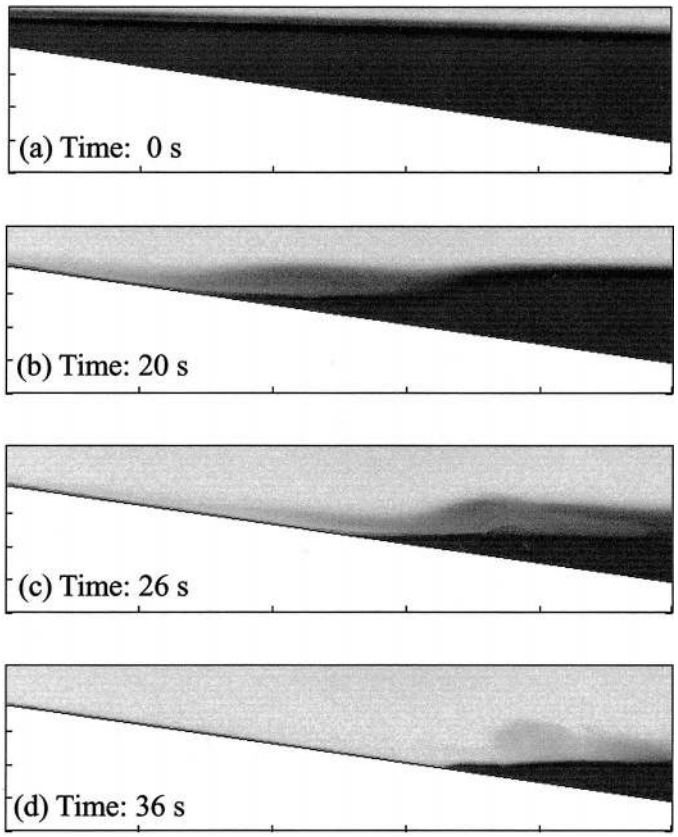

Fig. 7. Images of mixing as the layer interface advances along the slope for $t > 0$. Data from experimental run 6. The horizontal window length is 1 m and the aspect ratio is 1:1. The upper layer density $\rho_1 \approx 1{,}000$ kg m^{-3}, and the lower layer density $\rho_2 \approx 1{,}020$ kg m^{-3}.

of sloping topography, the energy in the ISW packet was ultimately lost to viscosity on time scales of order $3T_i$ to $5T_i$.

Figure 6c,d shows results for case 2, upwelling on boundary slopes of 3/20 and 1/10, respectively. In both panels, the evolution of E_{ISW}/PE_o was initially analogous to case 1 with no slope; however, now the waves shoaled after traveltimes of $0.5T_i$, $1.5T_i$, and $2.5T_i$. The first wave/slope interaction occurred at $0.5T_i$, prior to the development of any high-frequency ISWs (i.e., $t < T_s$). At this time, there was no discernible breaking of the basin-scale surge (with a mild wave slope) on the relatively steep boundary slope. The character of the second wave-slope interaction was dependent on the magnitude of $\alpha\eta_o/c_o$. For $\alpha\eta_o/c_o > 0.5$, we find $T_s < 1.5T_i$, which results in nearly all ISW energy (as much as 25% of PE_o) being lost near the boundary or reflected during the $1.5T_i$ shoaling event. For some experiments where $\alpha\eta_o/c_o \approx 0.5$, secondary breaking events were observed at $2.5T_i$. Experimental visualization revealed that these events transpired when the ISW packet had not fully developed before the primary breaking event (i.e., $T_s \approx 1.5T_i$); hence, subsequent packet development occurred prior to $2.5T_i$.

In Fig. 6e,f, results are shown for case 3, the initial condition of downwelling at boundary slopes of 3/20 and 1/10, respectively. Again, the evolution of E_{ISW}/PE_o is initially similar to the case with no slope but the waves then shoaled around T_i and $2T_i$. By $t \approx T_i$, wave steepening had begun, E_{ISW}/PE_o energy levels were about 5–10%, and this energy was lost from the ISW field at the boundary. As with the case of upwelling at the slope, for $\alpha\eta_o/c_o \approx 0.5$, a secondary breaking event may occur at $2T_i$.

It is clear from Fig. 6 that the forcing direction (upwelling or downwelling) determines the travel time of the ISW packet until it shoals, as a multiple of $T_i/2$. Similarly, the growth of the ISW packet is governed by T_s. The key nondimensional parameter, relative to the traveltime, is T_s/T_i (Fig. 6). From Eqs. (3) and (5), this parameter is

$$\frac{T_s}{T_i} = \frac{1}{3}\frac{h_1 h_2}{(h_1 - h_2)\eta_o} \tag{14}$$

We note that in Fig. 6c,d, the maximum $E_{ISW}/PE_o \approx 20\%$ occurred at $\alpha\eta_o/c_o \approx 0.5$; whereas in Fig. 6b, the maximum $E_{ISW}/PE_o \approx 20\%$ occurred at $\alpha\eta_o/c_o \approx 1$. Experimental visualization suggests that the slight reduction in wave-field energy as $\alpha\eta_o/c_o \to 1$ for the experiments with upwelling along the topographic slope may have resulted from enhanced energy transfer to mixing and dissipation as the density interface accelerated along the slope from the initial rest condition (Fig. 7). This mixing did not occur during the experiments with vertical end walls.

Breaker observations—Following the success of classifying surface breakers according to the Iribarren number, we found it instructive to test these classifications for internal wave breaking. Measurements of a_∞ and λ_∞ were obtained from the wave-gauge data at wave-gauge B. Images from the CCD camera were used to estimate a_b and classify the breaker type. In Figs. 8 and 9, internal waves are shown to spill, plunge, and collapse, suggesting that a form of the Iribarren classification may be suitable for internal wave breaking.

Spilling breakers were observed on the milder slope ($S = 1/10$), when the wave steepness is high ($\alpha\eta_o/c_o > 0.8$). Two examples of spilling breakers are presented in Fig. 8a–f and g–l. In both examples, the rear face of each ISW in the packet breaks as a wave of elevation in a spilling manner. Mixing and dissipation appear to be very localized and on occasion (e.g., Fig. 8c), baroclinic motions shear off the crest of the wave. These observations are similar to those by Helfrich (1992, his figs. 3–5).

Plunging breakers were observed on both slopes for moderately steep waves ($0.4 < \alpha\eta_o/c_o < 0.8$). Plunging occurred primarily during the breaking events at $1.5T_i$ in Fig. 6c,d. The initial condition of upwelling on the slope allowed a long travel time ($1.5T_i$) and a fully developed wave packet. Recall that, in these breaking events, up to 20% of the PE_o is lost from the high-frequency ISW field. Two examples of spilling breakers (Fig. 8m–r and s–x) suggest these events are more energetic than the spilling class. In each example, an intact mass of fluid from the rear face of each solitary wave of depression was observed to plunge foreward (e.g., Fig. 8o and u), becoming gravitationally unstable and forming a core of mixed fluid, which propagates upslope. These observations are similar to numerical results by Vlasenko and Hutter (2002, their fig. 6).

Collapsing breakers were also observed to occur on both boundary slopes, when the incident wave slope was milder than that required for plunging. Two examples of collapsing breakers (Fig. 9a–f and g–l) show that the breaking events were less energetic than plunging and were characterized by a mass of fluid beginning to plunge forward (e.g., Fig. 9d and i), and then collapsing down upon itself (e.g., Fig. 9e, and j–k). Compared with plunging breakers, little mixing occurred. These observations are similar to those by Michallet and Ivey (1999, their fig. 3).

For experiments where $h_1 = h_2$, $\alpha = 0$, and first-order KdV type solitary waves are prohibited from forming. Sufficiently strong forcing ($\eta_o/h_1 > 0.4$) may, however, generate supercritical flow conditions and an internal undular bore (see Horn et al. 2001). The large baroclinic shear associated with this forcing was capable of generating Kelvin–Helmholtz instability, both in the tank interior (Horn et al. 2001, their fig. 8) and at the boundary (Fig. 9m–r and s–x). Breaking of the undular waves through shear instability was observed to result in strong mixing of the water column (Fig. 9r,x). These observations are qualitatively similar to oceanic field observations by Moum et al. (2003, their fig. 14) and Orr and Mignerey (2003, their fig. 9).

Breaker classification and reflection coefficient—The breaker visualizations, as presented above, allow classification of the breaker type in terms of ξ and the measured reflection coefficient, $R = E_r/E_i$, where E_r and E_i are the energy in the reflected and incident wave packets, respectively, calculated from the wave-gauge B signal. The signal is not filtered in order to allow for the observed upscale energy transfer from the breaking high-frequency wave packet to a reflected longwave, which scales as the packet length (reflected long-wave energy would be removed by the filter employed in Fig. 6). Our experimental methodology did not permit calculation of the mixing efficiency Γ for a particular wave breaking event. However, Γ may be obtained from published observations of breaking lone solitary waves (Michallet and Ivey 1999, their fig. 10), when expressed as a function of ξ.

In Fig. 10a–c, we plot R versus ξ_b, ξ_∞, and ξ_{sech}, respectively. For small ξ, the wave slope is steep relative to S and the wave propagation over the slope approaches that of a wave in a fluid of constant depth, spilling breakers are observed, $R \to 0$, and viscosity dominates, with minimal wave energy converted to an increase in the potential energy of the system through diapycnal mixing (Fig. 10d,e). Conversely, for waves with very large ξ, the time scale of wave–slope interaction is small, $R \to 1$, and the collapsing breakers again induce minimal mixing. The inertia of these waves appears unable to overcome the stabilizing effect due to buoyancy. Intermediate to these extremes, plunging breakers develop with gravitational instabilities that drive mixing efficiencies, peaking near 25%. As the incident waves contain as much as 25% of the PE_o, it implies that 6% of the PE_o may be converted by diapycnal mixing to an irreversible increase in potential energy. These results are consistent with those for lone solitary waves by Michallet and Ivey (1999), which have been recast in terms of ξ and are also presented in Fig. 10b,c. The present results, however, have distinctly lower R values. This may be attributed to the observation that decaying turbulence and wave reflection associated with the leading wave generally interferes with subsequent waves in the packet, increasing fluid straining and therefore dissipation within the breaker. For this same reason, the breaker type classifications strictly apply to only the leading wave in each packet. Some differences, between these results and those of Michallet and Ivey (1999), might also arise from the presence of a no-slip boundary condition at the top surface (Redekopp pers. comm.).

Interpretation of our results, in terms of the mixing model by Ivey and Imberger (1991), suggests that, in the spilling and collapsing regions, mixing is suppressed by viscosity and buoyancy, respectively; consequently $\Gamma < 15\%$. In the plunging region, inertia dominates, suggesting that the scale of the most energetic overturns approaches the Ozmidov scale. As a result, the potential energy available for mixing is maximized and $\Gamma > 15\%$. Such large-scale overturning is also observed for Kelvin–Helmholtz billowing (Imberger and Ivey 1991) and critical internal wave breaking (Ivey and Nokes 1989).

The breaking point—Now that breaker classification guidelines have been established and the energy loss at the slope has been quantified, it is useful to estimate the position along the slope where breaking occurs (breaking point).

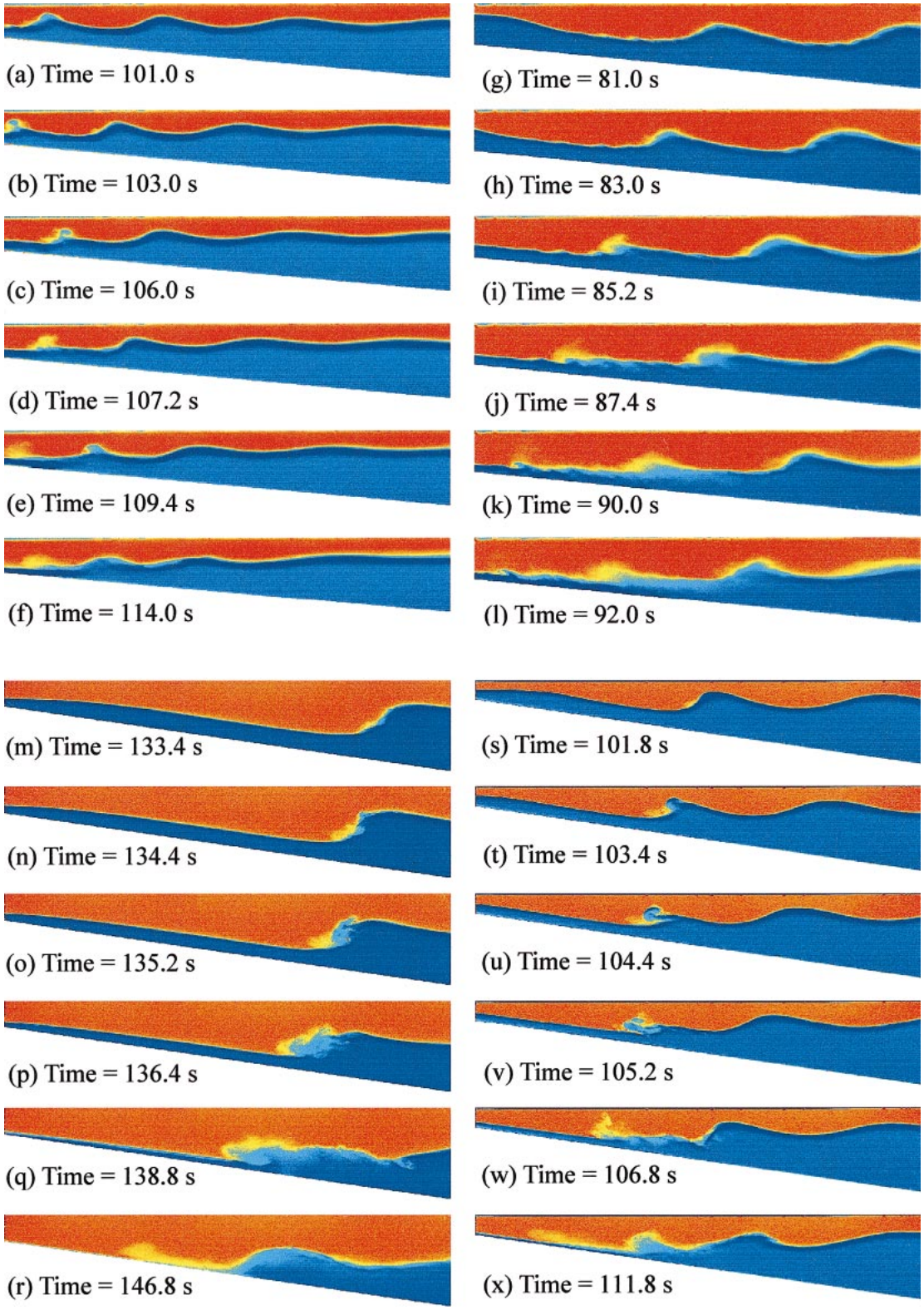

Fig. 8. False color images of spilling breakers: (a–f) run 28, (g–l) run 32. False color images of plunging breakers: (m–r) run 6, (s–x) run 12. The horizontal window length is 1 m and the aspect ratio is 1:1. The upper layer density $\rho_1 \approx 1{,}000$ kg m^{-3}, and the lower layer density $\rho_2 \approx 1{,}020$ kg m^{-3}.

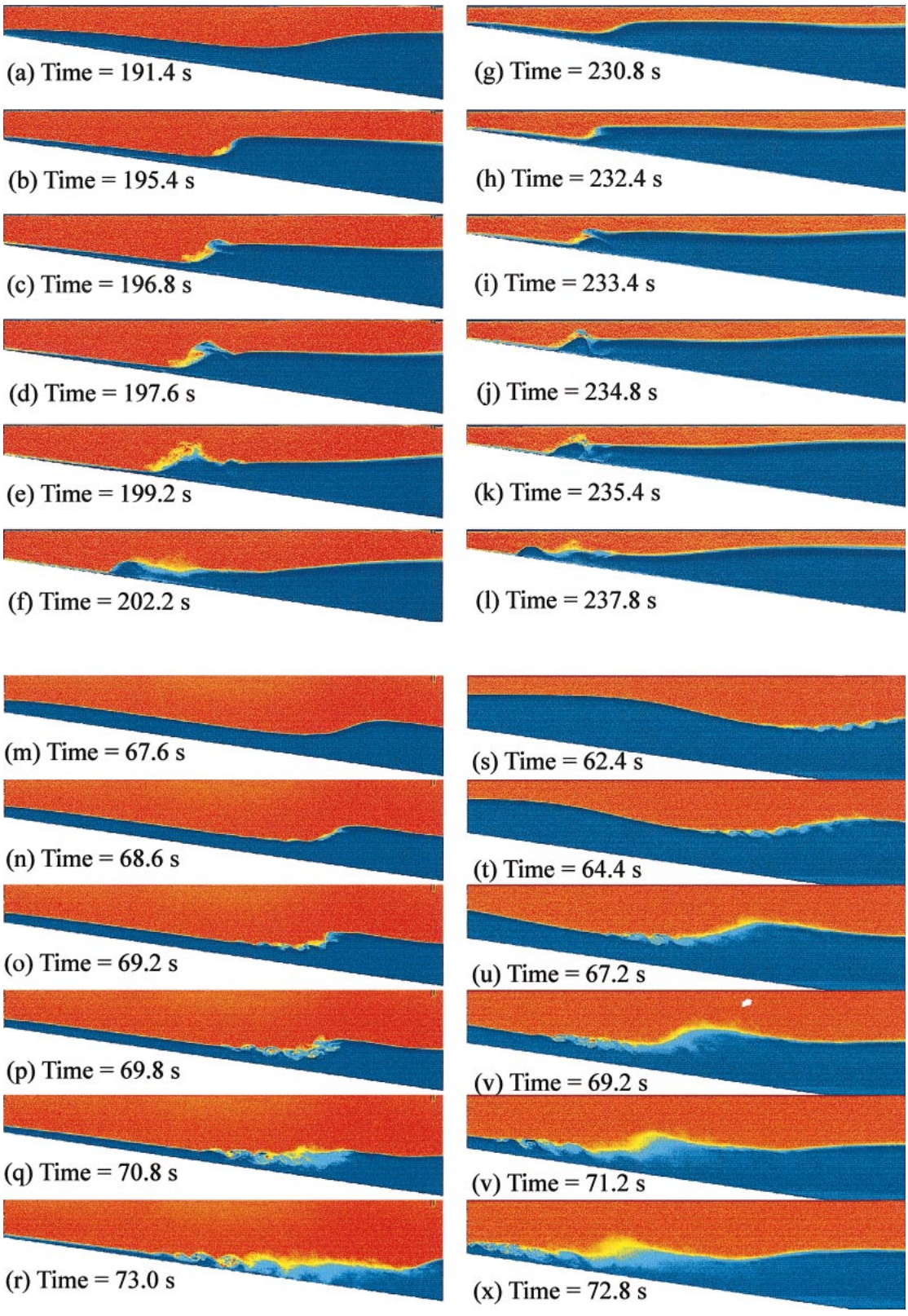

Fig. 9. False color images of collapsing breakers: (a–f) run 14, (g–l) run 11. False color images of Kelvin–Helmholtz breakers: (m–r) run 17, (s–x) run 18. The horizontal window length is 1 m and the aspect ratio is 1:1. The upper layer density $\rho_1 \approx 1{,}000$ kg m^{-3}, and the lower layer density $\rho_2 \approx 1{,}020$ kg m^{-3}.

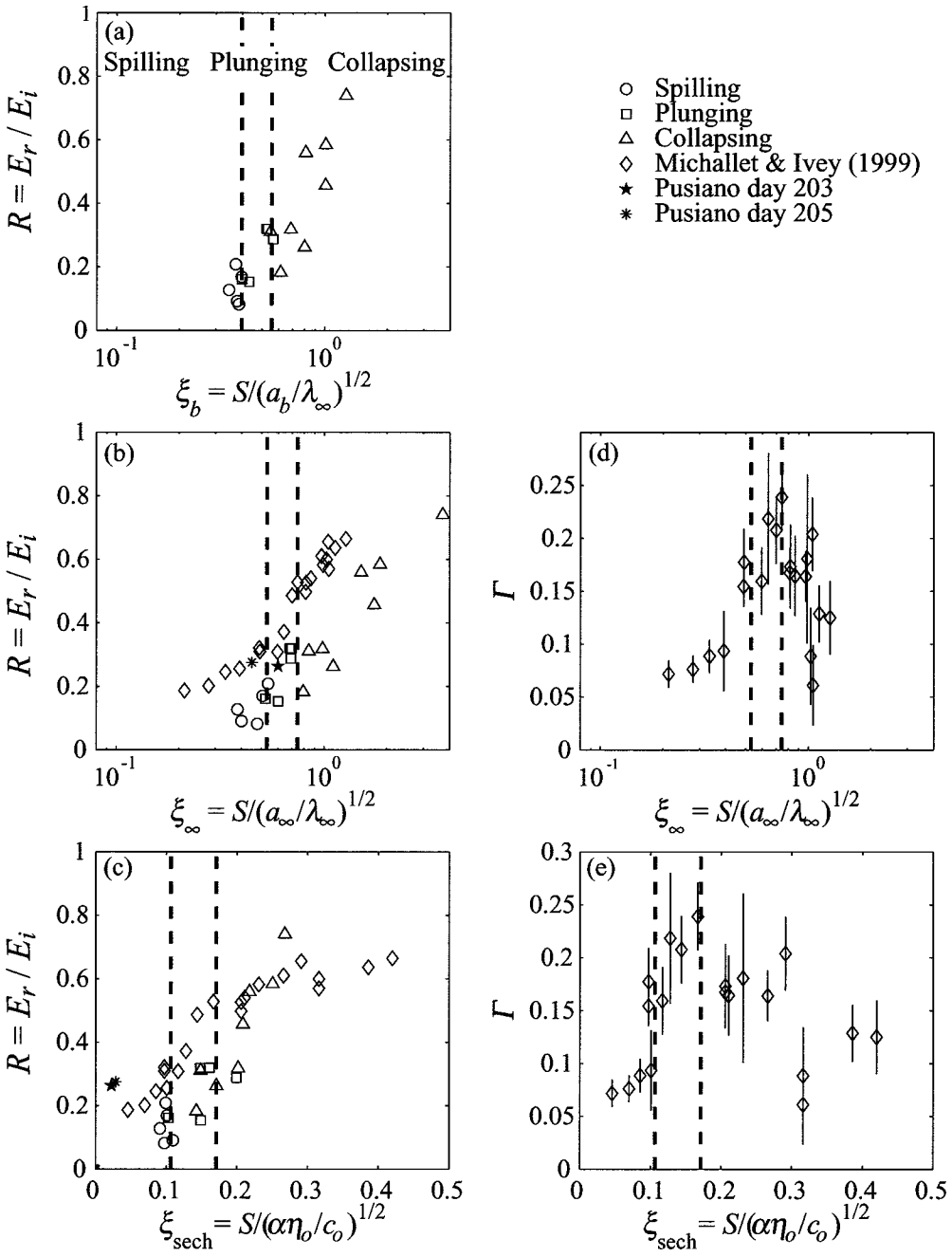

Fig. 10. Reflection coefficient (R), mixing efficiency (Γ), and breaker type classified according to the various forms of the Iribarren number: (a) Breaker type and R versus ξ_b, (b) breaker type and R versus ξ_∞, (c) breaker type and R versus ξ_{sech}, (d) breaker type and Γ versus ξ_∞, and (e) breaker type and Γ versus ξ_{sech}. The dashed lines demarcate the breaker classifications and are inferred in (d) and (e) from (b) and (c), respectively. The Γ observations in (d) and (e) are from Michallet and Ivey (1999).

Most studies to date have been concerned with the mechanics (e.g., Kao et al. 1985; Lamb 2002; Legg and Adcroft 2003) and location (e.g., Helfrich and Melville 1986; Vlasenko and Hutter 2002) of wave breaking upon the slope–shelf topography characteristic to the coastal ocean. Comparatively fewer studies have considered the propagation and breaking of ISWs over a topographic ridge (e.g., Farmer and Armi 1999; Sveen et al. 2002). Relevant to the present study, shoaling ISWs on closed slopes have been examined in the laboratory by Wallace and Wilkinson (1988) and Helfrich (1992). However, in the former study, a turning point was not encountered as $h_2 < h_1$. Helfrich (1992) determined a breaking criterion in terms of the undisturbed lower-layer depth at the breaking point h_b and the distance from the

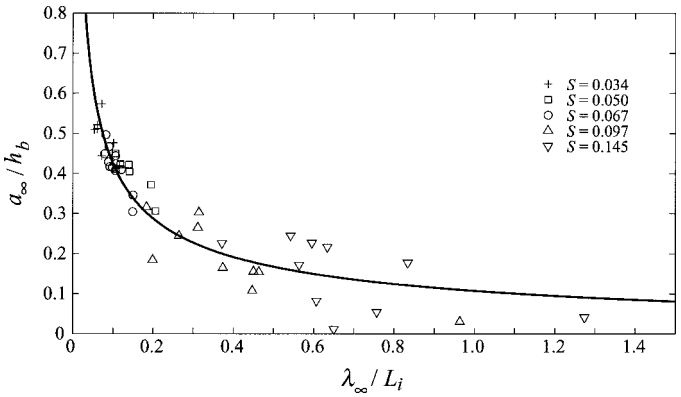

Fig. 11. The breaking point (criterion) as a function of the undisturbed lower layer depth (h_b). L_i is the distance from the beginning of the slope to the undisturbed interface–slope intersection. The experiments with slope, $S = 0.034$, 0.050, and 0.067 are from Helfrich (1992, his fig. 6).

beginning of the slope to the undisturbed interface–slope intersection, L_i. In Fig. 11, the breaking points for the present experiments (as observed from the CCD camera) are shown to complement these results. The tendency for a_∞/h_b to increase as λ_∞/L_i decreases is found to also be valid for steeper slopes, supporting the observation that larger waves tend to propagate into slightly shallower water (relative to their initial amplitude) before breaking (Helfrich 1992). An increase in bed-slope with λ_∞/L_i is also evident. The excursion of the interface along the slope and enhanced interfacial shear associated with the basin-scale seiche are likely responsible for the observed scatter in the breaking points of the present study, relative to (Helfrich 1992). The line of best-fit to the data

$$\frac{a_\infty}{h_b} = \frac{0.14}{(\lambda_\infty/L_i)^{0.52}} - 0.03 \tag{15}$$

allows generalization of the results.

An analytical breaking criterion was derived from Eq. (6), using the variable coefficients α and β that are dependent on the local fluid depth (e.g., Djordjevic and Redekopp 1978). This first-order weakly nonlinear form of KdV theory does not permit wave breaking (Whitham 1974) and is also limited to relatively steep slopes, where breaking occurs rapidly; thus, higher order nonlinear effects predominate over a relatively short transition zone. For details of the analysis, the reader is referred to Boegman (2004).

The observations presented thus far show the internal solitary waves of depression to ultimately break as waves of elevation. Before breaking, these waves must change polarity by passing through the turning point (beyond which $\alpha > 0$). This is shown to occur in Fig. 12, where the observed location of the breaking point is consistently after the theoretical prediction for the location of the turning point. Note that Eq. (10) is strictly appropriate for an undisturbed two-layer stratification and does not account for the excursion of the interface along the slope and enhanced interfacial shear associated with the basin-scale seiche.

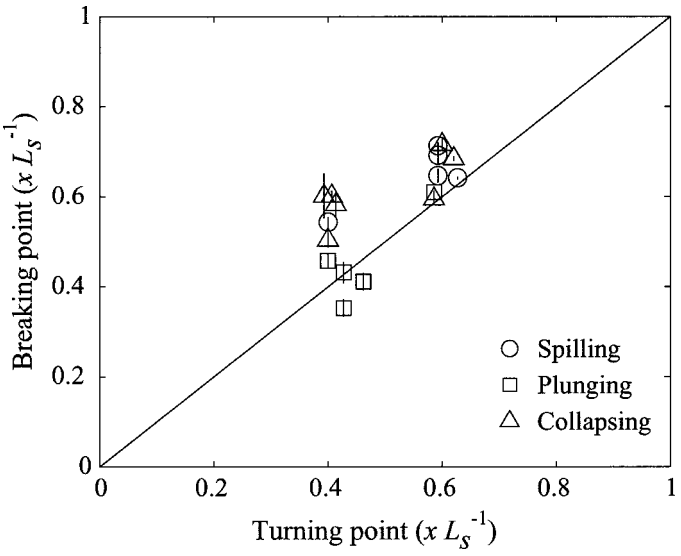

Fig. 12. Theoretical turning point versus measured breaking point. Various breaker types are shown: spilling, collapsing, and plunging. Error bars denote uncertainty in determining the breaking point due to parallax (shows maximum and minimum position).

Field observations

Lake Pusiano—To assess the applicability of our results, we applied our analysis to some recent observations from a lake with suitable field data and topography (Lake Pusiano, Italy; Fig. 13). This small, seasonally stratified lake, with near vertical and gradually sloping bathymetry on the north and south shores, respectively, is subject to pulses of high wind stress from the northerly direction (Fig. 14a). The episodic wind events, on days 203 and 205, introduce energy to the lake at the basin scale. For these events, $T_w > T_i/4$ and a general thermocline tilt is expected. Using the observed wind velocity, $W^{-1} = \eta_o/h_1$ was calculated (Table 2) from Eqs. (1) and (2). Following Stevens and Imberger (1996), the wind stress during each wind event was averaged and integrated over $T_i/4$. The response of the internal wave field to these wind events, as observed at station T, is con-

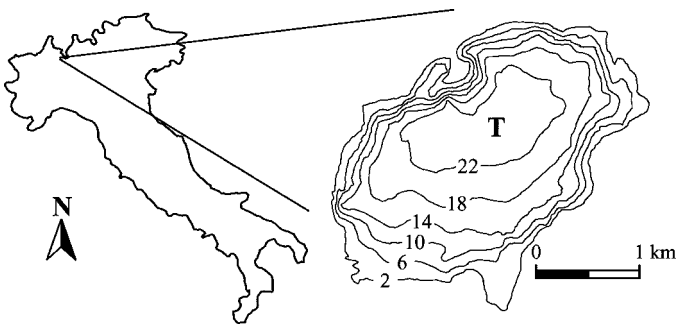

Fig. 13. Map showing the position of Lake Pusiano in Italy (48.80°N, 9.27°E) and the lake bathymetry. A thermistor chain (individual sensors every 0.75 m between depths of 0.3 and 24.3 m) and weather station (2.4 m above the surface) were deployed at station T during July 2003. Data were sampled at 10-s intervals. Isobaths are given in meters.

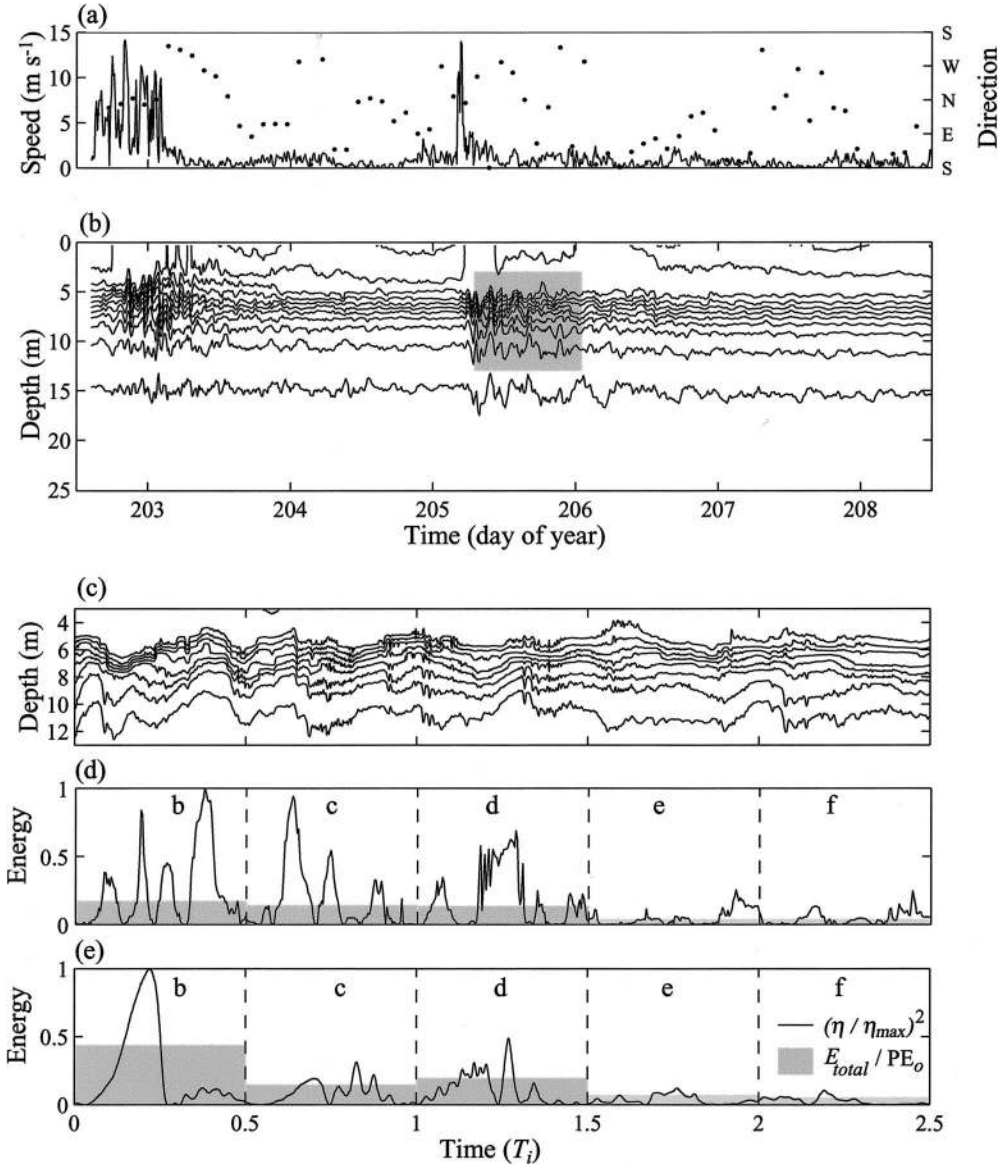

Fig. 14. Observations of wind speed and direction and isotherm displacement from Lake Pusiano at T. (a) Mean hourly wind direction (dots), and 10-min average wind speed (solid line), corrected to 10 m above the surface; (b) isotherms at 2°C intervals calculated through linear interpolation of thermistor data at T (10-min average); (c) detail of shaded region in (b) (1-min average). Note change of time base. The bottom isotherm in (b) and (c) are 8°C and 10°C, respectively. (d) Normalized instantaneous energy calculated as $c_o g(\rho_2 - \rho_1)\eta_{20}^2$ from the displacement of the 20°C isotherm (η_{20}) in (c) and the integral of this quantity shown as a fraction of the PE$_o$ over $T_i/2$ intervals as shown (see Table 2). PE$_o$ calculated assuming a linear η_{20} tilt of maximum excursion given by Eq. (1). (e) Same as (d) except for the layer interface from experimental run 31 rather than η_{20}. Letters b through f denote corresponding panels in Fig. 5.

sistent with other published field observations (e.g., Hunkins and Fliegel 1973; Farmer 1978; Boegman et al. 2003). Specifically, the generation and subsequent rapid dissipation of high-frequency internal waves was observed (Fig. 14b). To directly compare these observations to the laboratory results, an approximation to a two-layer stratification was made by separating the epilimnion from the hypolimnion at the 20°C isotherm (η_{20}). The nonlinear waves were isolated from contamination, due to motions at the basin scale and buoyancy frequency, by low-pass filtering and detrending η_{20}. The total energy was then integrated over the period of a progressive wave packet $T_i/2$

$$E_{\text{total}} = c_o g(\rho_2 - \rho_1) \int_{t_o}^{t_o + T_i/2} \eta_{20}^2(t)\, dt \qquad (16)$$

(*see* Boegman et al. 2005). The observed temporal evolution of η_{20}^2 and E_{total} (Fig. 14c,d) are similar to laboratory data

Table 2. Tabulated list of field observations together with the calculated parameters used in this study. With the exception of Lake Pusiano, the observations of η_0 are from (Horn et al. 2001, their table 1). Parameters calculated directly from observations in Lake Pusiano (Fig. 14) are denoted by ‡. R and Γ were estimated from Fig. 10b–e. N/A denotes a parameter that is not applicable. The — symbol denotes that data, while applicable, were not available.

Location	S	h_1 (m)	h_2 (m)	a_∞ (m)	f (Hz)	λ_∞ (m)	η_0 (m)	ξ_{sech}† or ξ_{sin}*	ξ_∞	R (%)	Γ (%)	Source
Bodensee	1/100	30	75	10	2.3×10^{-5}	6,500	—	—*	0.3	20	5–10	Unpubl. data (2001)
Kootenay Lake	1/20	30	65	5	1.4×10^{-4}	2,520	15	0.6*	1	50	5–25	Wiegand and Carmack (1986)
Lake Pusiano (day 203)	1/50	7	17	2	1.5×10^{-4}	2,130	3.4‡	0.5*	0.6	28‡	15–20	Fig. 14
Lake Pusiano (day 205)	1/50	7	17	2	2.7×10^{-4}	1,150	3.0‡	0.4*	0.4	26‡	5–15	Fig. 14
Kootenay Lake	1/20	30	65	5	2.8×10^{-4}	1,260	15	0.5*	0.8	40	20–25	Wiegand and Carmack (1986)
Sulu Sea	1/11	170	3,300	65	3.7×10^{-4}	6,300	N/A	—†	0.9	40	15–20	Apel et al. (1985)
Loch Ness	1/20	35	115	12	4.2×10^{-4}	880	12	0.08†	0.4	20	5–15	Thorpe et al. (1972)
Babine Lake	1/300	20	147	10	4.2×10^{-4}	460	10	0.004†	0.02	—	—	Farmer (1978)
Babine Lake	1/300	20	147	15	4.2×10^{-4}	460	10	0.004†	0.02	—	—	Farmer (1978)
Bodensee	1/100	25	75	20	5.8×10^{-4}	250	—	—†	0.04	—	—	Unpubl. data (2001)
North West Shelf	3/2,000	43	80	30	8.3×10^{-4}	910	N/A	—†	0.01	—	—	Holloway (1987)
North West Shelf	3/2,000	48	75	35	8.3×10^{-4}	830	N/A	—†	0.01	—	—	Holloway (1987)
Strait of Gibraltar	N/A	40	960	40	1.1×10^{-3}	—	N/A	—†	—	—	—	Ziegenbein (1969)
Lake Biwa	1/20	12	38	12	1.5×10^{-3}	460	12	0.05†	0.3	10–20	5–10	Boegman et al. (2003)
Oregon Shelf	—	7	140	21	1.6×10^{-3}	—	—	—†	—	—	—	Stanton and Ostrovsky (1998)
Seneca Lake	1/16	20	68	20	1.7×10^{-3}	210	10	0.09†	0.2	10–20	5–10	Hunkins and Fliegel (1973)
Massachusetts Bay	1/200	7	75	10	2.1×10^{-3}	422	N/A	—†	0.03	—	—	Halpern (1971)
Massachusetts Bay	1/200	7	75	10	2.8×10^{-3}	317	N/A	—†	0.03	—	—	Halpern (1971)
Scoatian Shelf	1/200	50	100	30	5.3×10^{-3}	1,100	N/A	—†	0.01	—	—	Sandstrom and Elliott (1984)
St. Lawrence	1/25	9	61	16	6.5×10^{-3}	124	N/A	0.03†	0.1	6–8	—	Bourgault and Kelley (2003)
Lake Kinneret	N/A	15	17	2	6.3×10^{-3}	30	N/A	N/A	N/A	—	—	Boegman et al. (2003)
Lake Kinneret	N/A	12	20	3	6.3×10^{-3}	30	N/A	N/A	N/A	—	—	Boegman et al. (2003)

from an experiment (run 31) with comparable initial and boundary conditions as shown in Fig. 14e (downwelling on slope, $h_1/H \approx 0.3$ and $0.4 < \eta_o/h_1 < 0.5$). During $0 < t < 0.5T_i$, the field and laboratory data show $E_{total}/PE_o \approx 20\%$ and $E_{total}/PE_o \approx 40\%$, respectively. The lower energy levels in the field appear to be attributed to the absence of a progressive nonlinear surge, which, in the laboratory, carried the high-frequency waves. During $0.5T_i < t < 1.5T_i$, the high-frequency oscillations in both systems contain approximately 15% of E_{total}/PE_o, and this energy rapidly decreases to approximately 5% as $t > 1.5T_i$.

Figure 5 allows the wave degeneration process in Lake Pusiano to be conceptually depicted. The initial condition, a northerly wind and sloping southern shore, was as shown in Fig. 5a. Upon termination of the wind stress, the system evolves schematically as shown in Fig. 5b–f. A long wave initially propagates from the upwelled fluid volume toward the sloping topography (Fig. 5b). This wave reflects from the slope and travels back toward the vertical wall (Fig. 5c), reflecting once more and steepening as it travels. Upon returning toward the slope, a high-frequency wave packet has formed with $E_{total}/PE_o \approx 15\%$ (Fig. 5d). These waves break upon the slope losing ~10% of the PE_o to local turbulent dissipation and mixing (Fig. 5e).

The observed energy loss at the slope in Pusiano may be compared with the predicted energy loss using the internal Iribarren model put forth in Fig. 10. The nondimensional parameters ξ_∞, ξ_{sech}, and E_r/E_i were calculated from the field data on days 203 and 205. In Fig. 10b, the parameter ξ_∞ is shown to be an accurate measure of E_r/E_i in both the field and in the laboratory. Spilling and plunging breakers are predicted, with the field measurements being grouped among the laboratory data collected in this study and that from Michallet and Ivey (1999). Conversely, the parameter ξ_{sech} is shown to overestimate the energy loss upon the slope in Pusiano relative to the laboratory model in Fig. 10c. Inspection of Fig. 14c and Table 2 reveals that the wind forcing is moderate (i.e., $W^{-1} \approx 0.4$); consequently, the high-frequency waves in Pusiano are sinusoidal in profile and thus will possess a greater wave length than that given for a sech^2 profile by Eq. (8b). In Fig. 10c, underestimation of the actual wave length (and hence overestimation of the wave slope) will result in a spurious decrease in ξ_{sech} and corresponding overestimation of E_r/E_i. For these waves, ξ_{sin} is more suitable.

An interpretation of the wave spectrum

A general model for the internal wave spectrum in lakes was proposed by Imberger (1998). This model is analogous to the Garrett–Munk spectrum found in the oceanographic literature. We use the results presented herein and the recent work by Antenucci and Imberger (2001) and Boegman et al. (2003) to update this model for large lakes with a seasonal thermocline and a discernible frequency bandwidth between the motions at the basin and buoyancy scales (bandwidth > 10^2~10^3 Hz). The three main features of the internal wave spectrum are shown in Fig. 15a. First is the presence of discrete natural and forced basin-scale seiches at frequencies between zero and ~10^{-4} Hz. Second is the presence of instabilities, generated by the surface wind forcing and the baroclinic shear of the basin-scale motions in the lake interior, with frequencies ~10^{-2} Hz. The third feature is the intermediate portion of the spectrum, which is shown to be dominated by freely propagating nonlinear wave groups capable of breaking at the lake perimeter (depending on ξ). Moderate forcing ($0.3 < W^{-1} < 1$), and perhaps topography in rotational systems (Saggio and Imberger 1998; Wake et al. 2004), is required for excitation of these waves, which are observed to have sinusoidal profiles at ~10^{-4} Hz (Fig. 14c) and sech^2 profiles at ~10^{-3} Hz (Saggio and Imberger 1998; Boegman et al. 2003). It is interesting to note that Lake Kinneret, while strongly forced, does not appear to generate a strong nonlinear internal wave response; yet the spectral peak resulting from shear instability near ~10^{-2} Hz is enlarged relative to Biwa and Pusiano (Fig. 15a). Drawing on examples found in the literature, the behavior of the spectrum in the nonlinear 10^{-4} to 10^{-3} Hz bandwidth may be generalized according to the ratio of the wave height and the depth of the surface layer a/h_1 (or equivalently $\eta_o/h_1 = W^{-1}$ because $a \sim \eta_o$). This ratio is commonly used to gauge the nonlinearity of progressive internal waves (e.g., Stanton and Ostrovsky 1998). A consistent trend is found throughout observations from a variety of natural systems with differing scales. Figure 15b shows sinusoidal waves near 10^{-4} Hz and sech^2 waves near 10^{-3} Hz when $a/h_1 < 0.4$ and $a/h_1 > 0.4$, respectively. The waves associated with shear instability in Lake Kinneret are mechanistically and observationally inconsistent with this model ($a/h_1 \approx 0.2$ and ~10^{-2} Hz). The revised spectral model for stratified lakes is summarized in Table 3.

Combination of the observations in Fig. 15b and the ξ model presented in Fig. 10 suggest that, in lakes with moderate to steep boundary slopes, $10\% \leq R \leq 50\%$ and $5\% \leq \Gamma \leq 25\%$, in the Sulu Sea, $R \sim 40\%$ and $15\% \leq \Gamma \leq 20\%$ and, in the St. Lawrence estuary, $R \sim 6\%$ to 8% (Table 2). These calculations may differ by as much as 50% from those calculated using the ratio of the wave length to the slope length (e.g., Michallet and Ivey 1999; Bourgault and Kelley 2003) and are only applicable to waves shoaling into a closed slope at the depth of the pycnocline.

In stratified waterbodies, internal waves provide the crucial energy transfer between the large-scale motions forced by winds and tides and the small-scale turbulent dissipation and mixing along sloping boundaries. This energy flux occurs through downscale spectral transfer and shoaling of high-frequency internal waves along topography suited for wave breaking. In lakes, moderate wind forcing ($0.3 < \eta_o/h_1 < 1$) excites sub–basin-scale nonlinear wave groups that propagate throughout the basin. These wave groups are also tidally generated in coastal regions. In both systems, when $0.3 < \eta_o/h_1 \sim a/h_1 < 0.4$, the waves have frequencies near 10^{-4} Hz and a sinusoidal profile whereas, when $0.4 < \eta_o/h_1 \sim a/h_1 < 1$, the waves have frequencies near 10^{-3} Hz and a sech^2 profile.

Using laboratory experiments, we have quantified the down-scale spectral energy flux for closed basins with a two-layer stratification. High-frequency internal solitary waves evolve from the basin-scale motions as $t \geq T_s$ and contain up to 20% of the available potential energy introduced by

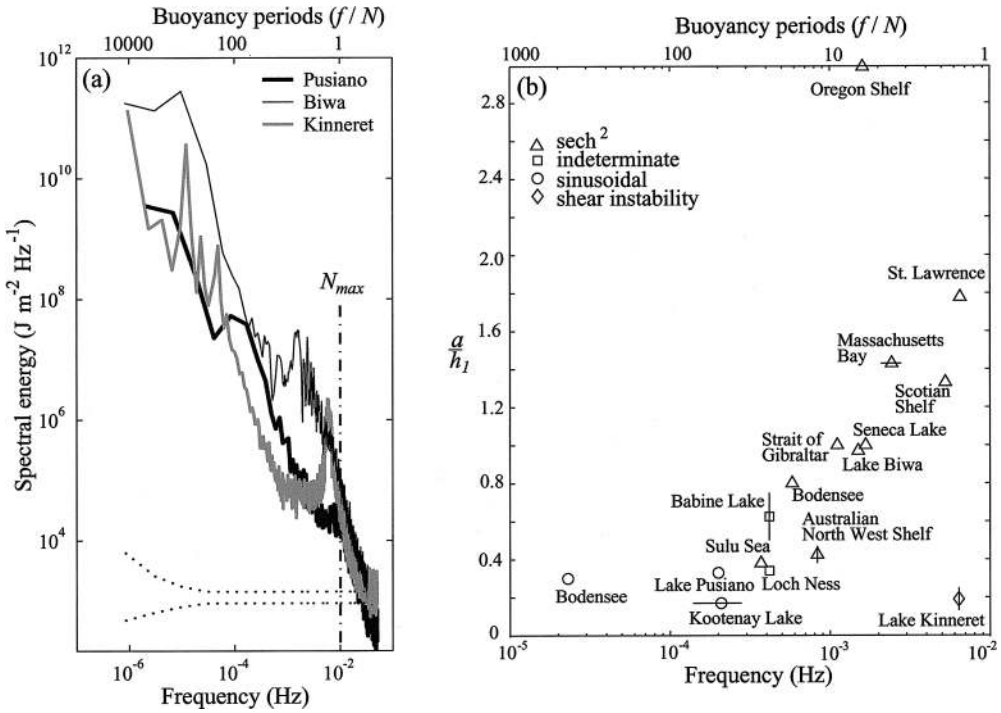

Fig. 15. (a) Spectra of the vertically integrated potential energy signal (*see* Antenucci et al. 2000) from Lake Pusiano (Fig. 14b) and lakes Kinneret and Biwa (see Boegman et al. 2003). The data were sampled at 10-s intervals and the spectra have been smoothed in the frequency domain to improve confidence at the 95% level, as shown by the dotted lines. N_{max} denotes the maximum buoyancy frequency. (b) Observations of wave nonlinearity, profile, and frequency from the literature. Sources are as given in Table 2. For buoyancy period calculations, we have assumed $N \sim N_{max} \sim 10^{-2}$ Hz.

the wind. As $T_i/2$ is the characteristic wave travel time over L, the ratio T_i/T_s describes the wave evolution and represents a balance between high-frequency wave growth through nonlinear steepening and high-frequency wave degeneration through shoaling at the boundary.

Wave breaking was observed at the boundary in the form of spilling, plunging, collapsing, and Kelvin–Helmholtz breakers. A single wave breaking event resulted in 10% to 75% of the incident wave energy being lost to dissipation and mixing, the remaining energy being found in a reflected long wave. The energy loss was dependent on the breaker type. Comparison with the results by Michallet and Ivey (1999) suggests that the mixing efficiency was also dependent on the breaker type and ranged between 5% and 25%. These boundary processes were modeled in terms of an internal Iribarren number ξ, defined as the ratio of the wave slope to the boundary slope. This definition is easily generalized to waves shoaling into a closed slope at the depth of the pycnocline in lakes, oceans, and estuaries. For closed basins, knowledge of the wave profile allowed ξ to be recast using properties of the quiescent fluid and the forcing dynamics.

Table 3. A revised spectral model for stratified lakes. Summarized from the data presented in Fig. 15.

Wave	Frequency (Hz)	Buoyancy periods
Linear basin scale	$<10^{-4}$	>100
Nonlinear sinusoidal profile	$\sim 10^{-4}$	~ 100
Nonlinear sech^2 profile	$\sim 10^{-3}$	~ 10
Shear instability	$\sim 10^{-2}$	~ 1
Maximum buoyancy frequency	$\sim 10^{-2}$	~ 1

Further study is required, as the laboratory facility did not permit examination of extremely mild slopes, such as those commonly found in many lakes and coastal oceans. These results will facilitate the parameterization of nonhydrostatic and sub–grid-scale wave processes into field-scale hydrodynamic models (e.g., Boegman et al. 2004).

References

ANTENUCCI, J. P., AND J. IMBERGER. 2001. On internal waves near the high frequency limit in an enclosed basin. J. Geophys. Res. **106:** 22465–22474.

———, J. IMBERGER, AND A. SAGGIO. 2000. Seasonal evolution of the basin-scale internal wave field in a large stratified lake. Limnol. Oceanogr. **45:** 1621–1638.

APEL, J. R., J. R. HOLBROOK, A. K. LIU, AND J. J. TSAI. 1985. The Sulu Sea internal soliton experiment. J. Phys. Oceanogr. **15:** 1625–1650.

BATTIES, J. A. 1974. Surf similarity. Proc. Coastal Engineering Conference, ASCE, **14:** 466–479.

BENNEY, D. J. 1966. Long nonlinear waves in fluid flows. J. Math. Phys. **45:** 52–63.

BOEGMAN, L. 2004. The degeneration of internal waves in lakes

with sloping topography. Ph.D. thesis, Centre for Water Research, The University of Western Australia.

———, J. IMBERGER, G. N. IVEY, AND J. P. ANTENUCCI. 2003. High-frequency internal waves in large stratified lakes. Limnol. Oceanogr. **48:** 895–919.

———, G. N. IVEY, AND J. IMBERGER. 2004. An internal solitary wave parameterization for hydrodynamic lake models. Proc. 15th Australasian Fluid Mechanics Conference.

———, ———, AND ———. 2005. The energetics of large-scale internal wave degeneration in lakes. J. Fluid Mech. **531:** 159–180.

BOURGAULT, D., AND D. E. KELLEY. 2003. Wave-induced mixing in a partially mixed estuary. J. Marine Res. **61:** 553–576.

COWEN, E. A., K.-A. CHANG, AND Q. LIAO. 2001. A single-camera coupled PTV-LIF technique. Exp. Fluids **31:** 63–73.

DJORDJEVIC, V. D., AND L. G. REDEKOPPP. 1978. The fission and disintegration of internal solitary waves moving over two-dimensional topography. J. Phys. Oceanogr. **8:** 1016–1024.

FARMER, D. M. 1978. Observations of long nonlinear internal waves in a lake. J. Phys. Oceanogr. **8:** 63–73.

———, AND L. ARMI. 1999. Stratified flow over topography: The role of small-scale entrainment and mixing in flow establishment. Proc. R. Soc. Lond. A **457:** 3221–3258.

FERRIER, A. J., D. R. FUNK, AND P. J. W. ROBERTS. 1993. Application of optical techniques to the study of plumes in stratified fluids. Dyn. Atmos. Oceans **20:** 155–183.

FISCHER, H. B., E. J. LIST, R. C. Y. KOH, J. IMBERGER, AND N. H. BROOKS. 1979. Mixing in inland and coastal waters. Academic.

FRICKER, P. D., AND H. M. NEPF. 2000. Buoyancy effects and internal seiche decay. Proc. International Symposium on Stratified Flow **5:** 313–318.

GALVIN, C. J. 1968. Breaker type classification on three laboratory beaches. J. Geophys. Res. **73:** 3651–3659.

GLOOR, M., A. WÜEST, AND D. M. IMBODEN. 2000. Dynamics of mixed bottom boundary layers and its implications for diapycnal transport in a stratified, natural water basin. J. Geophys. Res. **105:** 8629–8646.

GOUDSMIT, G.-H., F. PETERS, M. GLOOR, AND A. WÜEST. 1997. Boundary versus internal diapycnal mixing in stratified natural waters. J. Geophys. Res. **102:** 27903–27914.

HALPERN, D. 1971. Observations of short-period internal waves in Massachusetts Bay. J. Marine Res. **29:** 116–132.

HAMMACK, J. L., AND H. SEGUR. 1978. Modelling criteria for long water waves. J. Fluid Mech. **84:** 359–373.

HEAPS, N. S., AND A. E. RAMSBOTTOM. 1966. Wind effects on the water in a narrow two-layered lake. Phil. Trans. R. Soc. Lond. A **259:** 391–430.

HELFRICH, K. R. 1992. Internal solitary wave breaking and run-up on a uniform slope. J. Fluid Mech. **243:** 133–154.

———, AND W. K. MELVILLE. 1986. On nonlinear internal waves over slope-shelf topography. J. Fluid Mech. **167:** 285–308.

HODGES, B. R., J. IMBERGER, B. LAVAL, AND J. APPT. 2000. Modeling the hydrodynamics of stratified lakes. Proc. Hydroinformatics Conference **4:** 23–27.

HOLLOWAY, P. E. 1987. Internal hydarulic jumps and solitons at a shealf break region on the Austrailan North West Shelf. J. Geophys. Res. **92:** 5405–5416.

HORN, D. A., J. IMBERGER, AND G. N. IVEY. 1999. Internal solitary waves in lakes—a closure problem for hydrostatic models. Proc. Aha Huliko Hawaiian Winter Workshop—Internal Gravity Waves II **11:** 95–100.

———, ———, AND ———. 2001. The degeneration of large-scale interfacial gravity waves in lakes. J. Fluid Mech. **434:** 181–207.

———, L. G. REDEKOPP, J. IMBERGER, AND G. N. IVEY. 2000. Internal wave evolution in a space-time varying field. J. Fluid Mech. **424:** 279–301.

HUNKINS, K., AND M. FLIEGEL. 1973. Internal undular surges in Seneca Lake: A natural occurrence of solitons. J. Geophys. Res. **78:** 539–548.

IMBERGER, J. 1998. Flux paths in a stratified lake: a review, p. 1–18. *In* J. Imberger [ed.], Physical processes in lakes and oceans. Coastal and Estaurine Studies. V. 54.

———, AND G. N. IVEY. 1991. On the nature of turbulence in a stratified fluid. Part 2: Application to lakes. J. Phys. Oceanogr. **21:** 659–680.

IVEY, G. N., AND J. IMBERGER. 1991. On the nature of turbulence in a stratified fluid. Part 1: The energetics of mixing. J. Phys. Oceanogr. **21:** 650–658.

———, AND R. I. NOKES. 1989. Vertical mixing due to the breaking of critical internal waves on sloping boundaries. J. Fluid Mech. **204:** 479–500.

KAKUTANI, T., AND N. YAMASAKI. 1978. Solitary waves on a two-layer fluid. J. Phys. Soc. Japan **45:** 674–679.

KAO, T. W., F. S. PAN, AND D. RENOUARD. 1985. Internal solitons on the pycnocline generation, propagation, shoaling and breaking over a slope. J. Fluid Mech. **159:** 19–53.

KOMAR, P. D. 1976. Beach Processes and Sedimentation. Prentice-Hall.

LAMB, K. G. 2002. A numerical investigation of solitary internal waves with trapped cores formed via shoaling. J. Fluid Mech. **451:** 109–144.

LEDWELL, J. R., AND B. M. HICKEY. 1995. Evidence for enhanced boundary mixing in the Santa Monica basin. J. Geophys. Res. **100:** 20665–20679.

LEE, C. Y., AND R. C. BEARDSLEY. 1974. The generation of long nonlinear internal waves in a weakly stratified shear flow. J. Geophys. Res. **79:** 453–462.

LEGG, S., AND A. ADCROFT. 2003. Internal wave breaking at concave and convex continental slopes. J. Phys. Oceanogr. **33:** 2224–2246.

MACINTYRE, S., K. M. FLYNN, R. JELLISON, AND J. R. ROMERO. 1999. Boundary mixing and nutrient fluxes in Mono Lake, California. Limnol. Oceanogr. **4:** 512–529.

MICHALLET, H., AND E. BARTHÉLEMY. 1997. Ultrasonic probes and data processing to study interfacial solitary waves. Exp. Fluids **22:** 380–386.

———, AND G. N. IVEY. 1999. Experiments on mixing due to internal solitary waves breaking on uniform slopes. J. Geophys. Res. **104:** 13467–13477.

MILES, J. W. 1981. The Korteweg–de Vries equation: A historical essay. J. Fluid Mech. **106:** 131–147.

MONISMITH, S. G. 1987. Modal response of reservoirs to wind stress. ASCE J. Hydraul. Eng. **113:** 1290–1306.

MORTIMER, C. H. 1974. Lake hydrodynamics. Mitt. Internat. Verein. Limnol. **20:** 124–197.

———, AND W. HORN. 1982. Internal wave dynamics and their implications for plankton biology in the Lake of Zurich. Mitt. Internat. Verein. Limnol. **127:** 299–318.

MOUM, J. N., D. M. FARMER, W. D. SMYTH, L. ARMI, AND S. VAGLE. 2003. Structure and generation of turbulence at interfaces strained by internal solitary waves propagating shoreward over the continental shelf. J. Phys. Oceanogr. **33:** 2093–2112.

ORR, M. H., AND P. C. MIGNEREY. 2003. Nonlinear internal waves in the South China Sea: Observation of the conversion of depression internal waves to elevation internal waves. J. Geophys. Res. **108:** 3064. Doi:10.1029/2001JC001163.

OSTROVSKY, I., Y. Z. YACOBI, P. WALLINE, AND I. KALIKHMAN. 1996. Seiche-induced mixing: Its impact on lake productivity. Limnol. Oceanogr. **4:** 323–332.

SAGGIO, A., AND J. IMBERGER. 1998. Internal wave weather in stratified lakes. Limnol. Oceanogr. **43:** 1780–1795.

SANDSTROM, H., AND J. A. ELLIOTT. 1984. Internal tide and solitons on the Scotian Shelf: A nutrient pump at work. J. Geophys. Res. **89:** 6415–6426.

SPIGEL, R. H., AND J. IMBERGER. 1980. The classification of mixed-layer dynamics in lakes of small to medium size. J. Phys. Oceanogr. **10:** 1104–1121.

STANTON, T. P., AND L. A. OSTROVSKY. 1998. Observations of highly nonlinear internal solitons over the Continental Shelf. Geophys. Res. Lett. **25:** 2695–2698.

STEVENS, C., AND J. IMBERGER. 1996. The initial response of a stratified lake to a surface shear stress. J. Fluid Mech. **312:** 39–66.

SVEEN, J. K., Y. GUO, P. A. DAVIES, AND J. GRUE. 2002. On the breaking of internal solitary waves at a ridge. J. Fluid Mech. **469:** 161–188.

THOMPSON, R.O.R.Y., AND J. IMBERGER. 1980. Response of a numerical model of a stratified lake to wind stress. Proc. Intl. Symp. Stratified Flows **2:** 562–570.

THORPE, S. A. 1971. Asymmetry of the internal seiche in Loch Ness. Nature **231:** 306–308.

———, A. HALL, AND I. CROFTS. 1972. The internal surge in Loch Ness. Nature **237:** 96–98.

TORRENCE, C., AND G. P. COMPO. 1998. A practical guide to wavelet analysis. Bull. Amer. Meteor. Soc. **79:** 61–78.

VLASENKO, V., AND K. HUTTER. 2002. Numerical experiments on the breaking of solitary internal waves over a slope-shelf topography. J. Phys. Oceanogr. **32:** 1779–1793.

WAKE, G. W., G. N. IVEY, AND J. IMBERGER. 2004. The temporal evolution of baroclinic basin-scale waves in a rotating circular basin. J. Fluid Mech. **515:** 63–86.

WALLACE, B. C., AND D. L. WILKINSON. 1988. Run-up of internal waves on a gentle slope in a two-layered system. J. Fluid Mech. **191:** 419–442.

WHITHAM, G. B. 1974. Linear and nonlinear waves. Wiley.

WIEGAND, R. C., AND E. C. CARMACK. 1986. The climatology of internal waves in a deep temperate lake. J. Geophys. Res. **91:** 3951–3958.

WÜEST, A., G. PIEPKE, AND D. C. SENDEN. 2000. Turbulent kinetic energy balance as a tool for estimating vertical diffusivity in wind-forced stratified waters. Limnol. Oceanogr. **45:** 1388–1400.

ZHOU, X., AND R. GRIMSHAW. 1989. The effect of variable currents on internal solitary waves. Dyn. Atmos. Oceans **14:** 17–39.

ZIEGENBEIN, J. 1969. Short period internal waves in the Strait of Gibralter. Deep-Sea Res. **16:** 479–487.

Received: 3 August 2004
Accepted: 18 April 2005
Amended: 30 May 2005